Agenzia nazionale per le nuove tecnologie,
l'energia e lo sviluppo economico sostenibile

MINISTERO DELLO SVILUPPO ECONOMICO

Ricerca di Sistema elettrico

Validazione sperimentale e ottimizzazione di cristalli fotonici ibridi metallo-dielettrici come strati riflettori posteriori di celle fotovoltaiche a film sottile per migliorare l'intrappolamento della radiazione solare

A. Micco, G. Quero, A. Ricciardi, I. Usatii,
E. Bobeico, M. Pisco, A. Cusano,
V. La Ferrara, L.V. Mercaldo, L. Verdoliva, P. Delli Veneri

Università degli Studi del Sannio

Report RdS/2013/003

VALIDAZIONE SPERIMENTALE E OTTIMIZZAZIONE DI CRISTALLI FOTONICI IBRIDI METALLO-DIELETTRICI COME STRATI RIFLETTORI POSTERIORI DI CELLE FOTOVOLTAICHE A FILM SOTTILE PER MIGLIORARE L'INTRAPPOLAMENTO DELLA RADIAZIONE SOLARE

A.Micco[1], G. Quero[1], A. Ricciardi[1], I. Usatii[1], E. Bobeico[1], M. Pisco[1], A. Cusano[1], V. La Ferrara[2], L.V. Mercaldo[2], L. Verdoliva[2], P. Delli Veneri[2]
[1]Università degli Studi del Sannio, Dipartimento di Ingegneria – Divisione di Optoelettronica
[2]ENEA – UTTP MDB, C. R. Portici

Settembre 2013

Report Ricerca di Sistema Elettrico

Accordo di Programma Ministero dello Sviluppo Economico - ENEA
Piano Annuale di Realizzazione 2012
Area: Produzione di Energia Elettrica e Protezione dell'Ambiente
Progetto: Energia Elettrica da Fonte Solare – Ricerca su Celle Fotovoltaiche Innovative
Obiettivo: Sviluppo di materiali e architetture di dispositivo per celle solari tandem micromorfe

Responsabile del Progetto: Paola Delli Veneri, ENEA

Il presente documento descrive le attività di ricerca svolte all'interno dell'Accordo di collaborazione *"Cristalli fotonici ibridi metallo-dielettrici come strati riflettori posteriori di celle fotovoltaiche a film sottile per migliorare l'intrappolamento della radiazione solare"*

Responsabile scientifico ENEA: Vera La Ferrara
Responsabile scientifico Università del Sannio: Andrea Cusano

Index

SUMMARY 5

1 INTRODUCTION 6

2 DESCRIPTION OF ACTIVITIES AND RESULTS 7

2.1 *CASE OF STUDY* 7

2.1.1 *METHODOLOGY AND OBSERVABLES* 8

2.1.2 *INFLUENCE OF THE CELL GEOMETRY* 10

2.2 *FIBONACCI-LIKE BACKREFLECTOR* 11

2.2.1 *INFLUENCE OF THE AMORPHOUS SI OPTICAL PROPERTIES* 13

2.2.2 *REMARKS ON THE SUPERCELL APPROXIMATION AND THE SCALE RATIO T* 14

2.3 *INFLUENCE OF THE INCIDENCE ANGLE* 16

2.4 *EXPERIMENTAL SECTION* 17

2.4.1 *NANOPATTERNING ON N-SIOX:H* 17

2.4.2 TIME-DEPENDENT MILLING ON N-SIOX:H 18

2.4.3 REDEPOSITION AND ITS DEPENDENCE OF FIB MILLING PARAMETERS ON N-SIOX:H 19

2.4.3.1 *MILLING DIRECTION AND SCAN ROUTINE* 19

2.4.3.2 *MAGNIFICATION* 20

2.4.3.3 *DEPENDENCE OF DWELL TIME* 20

2.4.3.4 *DEPENDENCE OF NUMBER OF LOOPS* 21

2.4.3.5 *DEPENDENCE OF TOTAL ION DOSE ON MILLING* 22

2.4.4 SPUTTERING YIELD OF N-SIOX:H *NANOPATTERNING ON N-SIOX:H* 23

2.4.4.1 PREDICTION OF SPUTTERING YIELD BY TRIM 23

2.4.4.2 EXPERIMENTAL SPUTTERING YIELD FOR DIFFERENT BEAM CURRENTS AND ION DOSE 23

2.4.5 NANOPATTERNING OF ZNO LAYER 24

3 CONCLUSIONS 26

4 REFERENCES 28

5 CV OF THE UNIVERSITY INVESTIGATORS 31

Summary

This document covers the activities carried out during the project "EXPERIMENTAL VALIDATION AND OPTIMIZATION OF HYBRID METALLO-DIELECTRIC CRYSTALS USED AS BACKREFLECTOR IN THIN-FILM SOLAR CELLS TO IMPROVE THE SOLAR TRAPPING" carried out in collaboration between ENEA and University of Sannio.
The document is organized as follows: After an introduction about the state of the art of backreflectors in thin film solar cell, we present the solar cell models considered in our study and the numerical method used for calculating the light absorption (activity done by University). In particular with reference to a periodic metallic nanograting backreflector we discuss about the influence of the cell geometry on the light absorption enhancement due to the backreflector. Once selected the configuration which provides the highest absorption values we evaluate the light absorption enhancement due to a Fibonacci-like backreflector with respect to the periodic counterpart by also taking into account the influence of the a-Si optical properties. We study the dependence of the light absorption of both periodic and aperiodic case on the incidence angle. The rest of the sections deal with the experimental results (activity done by ENEA). In particular, the feasibility of different nanopatterning strategies proposed in the simulation work, using the Focused Ion Beam (FIB) as advanced nanolithography is verified. Micro-nanochannels have been realized both on n-SiOx:H film, used as the n-layer of the junction, and on ZnO layers, used as the front electrode of the device. In particular pin single junction amorphous silicon device has been realized starting from substrate glass/TCO structured by FIB in order to verify the feasibility of this technique. Finally we provide the conclusions.

1 Introduction

Thin film solar cells (with thickness ranging from hundreds of nm up to few µm) are attractive candidates for low-cost replacement of thick (150-300 µm) wafer-based devices, due to the reduced costs of raw materials and processing. Thin film silicon modules, made of amorphous (a-Si:H) and/or microcrystalline silicon (µc-Si:H), have the further advantage of relying on abundant non-toxic materials. A significant issue for such devices is to keep the silicon absorber layer as thin as possible in order to both reduce production time and costs and lessen the impact of the light induced degradation [1] thus improving the cell stability. Light trapping, making the cell "optically thick" despite the limited physical thickness, is then crucial to realize high efficiency solar cells and advanced photon management strategies have gained tremendous interest [2,3].

The light-trapping concept adopted for thin-film Si solar cells is presently based on randomly textured interfaces combined with a reflective back contact [4]. Optimization of morphologies and scattering characteristics is under intensive investigation [3-11]. This component has to provide for high reflectivity over a broad wavelength band and efficient scattering at large angles of the unabsorbed light, to prolong the optical paths back in the thin active layers. One conventional solution is the use of a metal back reflecting contact, like Ag with excellent conductivity and good reflectivity. In this case a thin buffer layer with low refractive index, like doped ZnO, is generally inserted between Si and Ag, but novel design are also under investigation[12-13].

As an alternative dielectric mirrors based on photonic crystals (PCs) have been proposed [14-15]. In fact, PCs in the form of dielectric multilayer structures (also known as Distribuited Bragg Reflectors (DBRs)) behave as perfect mirrors in the bandgap wavelength range [16,17]. This configuration, however, is in general unsuitable for thin films solar cells given the tens of dielectric layers necessary for achieving high reflectivity. In order to tailor the reflectance spectrum for achieving a better control of the operational wavelength range, PCs can be used (in the out-of-plane configuration) as diffraction gratings, able to couple incident light at specific wavelengths into resonant (photonic) modes that propagate along the plane of the cell [18]; in this configuration the PC-based backreflector is able to efficiently turn the incident light (at the resonant wavelength) by an angle of 90°, which can be guided and thus absorbed along the lateral direction of the cell thereby bypassing the problems relative to the its limited thickness. Furthermore, if the grating is composed by metals, in addition to the photonic modes, the incoming radiation can also couple to surface plasmon polaritons excited at the metal/semiconductor (i.e. the active region) interface [19,20]. In this way both the photonic and plasmonic resonances could contribute simultaneously to the light trapping process [21]. The excitation of both photonic and plasmonic modes is due to the fulfillment of the phase-matching conditions with the waves scattered by the grating, whose parameters can be effectively engineered for achieving the mode coupling just into the poorly absorbed wavelength range.

So far the research in this field has been principally focused on both periodic ordered PC structures (based on photonic/plasmonic crystals) and randomly disordered textured surfaces [4,22,23], however the latter solution is in practice limited by an uncontrollable engineering of the light scattering mechanism in the spectral region of enhancement. Deterministic quasiperiodic geometries could fill the gap between periodically and randomly ordered structures by retaining the essential characteristics of periodic-like light scattering mechanism while introducing a richer resonant spectrum [24-26]. This richness basically results in a phase matching condition fulfillment occurring at more wavelengths (corresponding to a larger number of excited resonant modes responsible for the light trapping) with respect to the periodic case. In this context, an interesting study on pseudorandom arrays of resonantly scattering nanoparticles for light trapping has been presented demonstrating that engineered random nanopatterns show a more isotropic response (and thus a less invariant absorption spectrum) with light incidence angle [22]. Recently a higher photocurrent enhancement compared to optimized periodic gratings structures has been experimentally

demonstrated by using cells coupled to aperiodic golden spiral arrays [27]. Moreover, in a recent work, we have exploited the richness of the spatial spectrum of quasiperiodic geometries in hybrid metallo-dielectric structures demonstrating that a Fibonacci-like nanograting used as backreflector in a thin film solar cell may yield up to 7% higher enhancements (against a maximum 2.7% loss) with respect to the periodic counterpart [28]. In the wake of this promising result, in this work we provide a comprehensive discussion on the light-trapping properties of quasi-periodic Fibonacci-like 1D backreflectors [29], comparing them with the standard periodic ones. Our analysis is carried out on a realistic case study, where light absorption is evaluated only within the intrinsic layer of the P-I-N junction forming the active region. First, three different cell configurations corresponding to different fabrication procedures are analyzed. For the configuration that guarantees the best absorption values we compare the performances of periodic and Fibonacci-like metal nanograting backreflectors, demonstrating that the amorphous silicon optical properties strongly influence the results of comparison. Overall, we found that aperiodic geometries are effectively able to offer advantages in terms of maximum achievable enhancement and more stable and isotropic absorption values for different incidence angle. Although the most used configurations are currently based on 2D patterns, the numerical study on 1D gratings is certainly more approachable (in terms of computational time and resources) and still allows to gather information on the physical phenomena associated with the periodic/aperiodic scattering surfaces. As concern the experimental activity (described in “Experimental section”) it has been used a system of advanced nanolithography, the Focused Ion Beam (FIB), to perform micro-nanopatterning both on n-SiOx film, used as the n-layer of the junction, and on ZnO layers, used as the front electrode of the device. The aim is to test the feasibility of different nanostructuring strategies for device prototyping.

2 Description of activities and results

2.1 Case of study

The proposed solar cell structures analyzed in this project are schematically shown in Fig. 1(a); similarly to [28] the cells essentially consist of a thick top layer of ZnO acting as transparent electrode, the a-Si:H P-I-N junction and the silver nanograting consisting of a periodic 1D grating (only one period i.e. the unit cell is shown) used as backreflector and bottom contact. An advanced n-type layer is considered in the solar cell, made of doped silicon oxide (n-SiOx) playing the dual function of doped layer in the P-I-N junction and dielectric spacer between silicon and silver [12,13].

It has been indeed recently demonstrated that the use of this material allows to remove the ZnO layer (80 nm thick) in the standard ZnO/Ag back reflector, thus allowing to minimize the distance between the light absorber (intrinsic a-Si:H layer) and the silver back reflecting contact. This configuration gives the opportunity to fully exploit the light trapping capability of the patterned back reflector where it is needed (active layer). The P-type region (usually very thin, ~ 10 nm) is neglected.

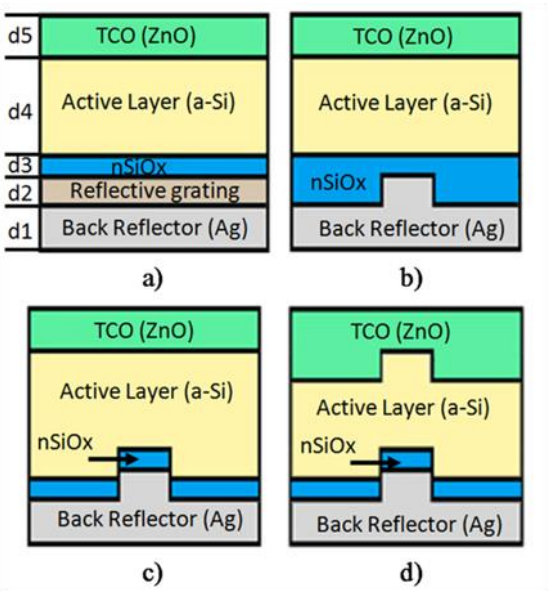

Figure 1. (a) Schematic of the solar cell with the definition of the layer's thickness values; (b), (c) and (d) schematics of three different configurations studied in the work.

In order to study the influence of the backreflector on the cell geometry, in the following we consider three configurations achievable with different top-down fabrication processes; the first one (schematized in Fig. 1(b)), requires the lithographic/etching step to be performed directly into the n-SiOx layer before the final silver deposition. In the second configuration, the lithographic/etching step is performed over the silicon layer before the successive n-SiOx deposition. In this case, the thin n-SiOx film is supposed to be deposited on both the ridges and grooves of the silicon grating before the final metal (silver) layer deposition. Fig. 1(c) shows the schematic of the final device. In the last configuration, the grating is firstly written in the ZnO layer and the successive conformal depositions of a-Si, n-SiOx and silver form the structure schematized in Fig. 1(d).

Although the structures in Fig. 1 can all be fabricated (please see “Experimental section” below), quite different electrical properties can be expected. In particular, etching into the active layer (case c) may induce surface damage in the etched region, resulting in high recombination losses. On the other hand, the growth onto surfaces with high roughness (case d) is known to favour the formation of structural defects (voids and nano-porous regions) with detrimental effect on cell voltage [30-32]. Nevertheless, the feasibility of solar cells on substrates patterned by nano-inprinting with minimal deterioration of the electrical parameters has been recently demonstrated [33]. Moreover, the integration of advanced silicon-oxide based doped layers, like the n-SiOx layer considered in our structures, has shown beneficial effects against the detrimental nanoporous-phase contribution [12,34]. These considerations should be kept in mind in the application, where the approach of maximizing the light absorption does not necessarily translate into improved cell performance. Anyway, a discussion about the experimental results achieved in this project is reported in “Experimental section”.

In the following, for each of these structures, starting from the simple periodic grating as backreflector, we have calculated the light absorption when the structure is illuminated by a normally incident plane wave; the absorption is evaluated only in the intrinsic layer of the P-I-N junction which is the layer devoted to light absorption.

2.1.1 Methodology and observables

In our numerical analysis and according to the activities carried out in the previous years, we have used the commercial software package Comsol© Multiphysics (RF module v. 3.5a) based on the finite element method [35].

Dispersive and lossy refractive index of Ag was taken from ref 36, while we modeled ZnO (1.96-0.002i @ 500 nm and 1.77-0.01i @ 950 nm), n-SiOx (2.58-0.04i @ 500 nm and 2.31-0i @ 950 nm) and a-Si (4.44-0.57i @ 500 nm and 3.41-0i @ 950 nm) according to spectroscopic ellipsometry measurements performed on films deposited on glass. The choice of the a-Si model is a delicate issue strongly affecting the light absorption values and thus determining the real usefulness of structured back-reflectors in thin film solar cells, as it will be discussed below.

The computational domain is limited by the grating unit cell (Fig 1(a)), horizontally terminated by periodic boundary conditions. At the top (air layer) and bottom (silver layer) boundaries are applied the port and the perfect electric conductor conditions, respectively.

Preliminarily, we checked the stability by performing a study on the mesh discretization of the computational domain. In fact, the singularity of the field occurring at the edge of the grating (particularly evident for the plasmonic resonances), causes a critical dependence of the numerical results on the mesh selection. As matter of fact, results accuracy and stability have thus been achieved at the cost of computational time by using a denser mesh (maximum element size less than 60 pm) in correspondence of the grating edges. For less 'critical' subdomains, the mesh maximum element size has been set to 1/50×300 nm, being 300 nm the lower operating wavelength in the investigated spectral range.

According to ref. 28 the light absorption A has been calculated as the flux of the Poynting vector (real part):

$$\mathrm{A} = \int_{\Sigma} \mathrm{Re}\left\{ \vec{S}\left(\vec{r},\omega\right)\right\} \bullet ds \tag{1}$$

where $\vec{S}\left(\vec{r},\omega\right)$ is the Poynting vector and the integration domain Σ is limited to the intrinsic region corresponding to the surface containing only the a-Si layer (excluding the n-SiOx layer at the bottom of the cell). The absorption has been evaluated for both TE (electric field polarized along the grating lines) and TM (electric field polarized perpendicular to the grating lines) polarizations, and the total absorption is simply evaluated as $A = 1/2\left(A_{TE} + A_{TM}\right)$.

As in ref.21,28, to numerically quantify the efficiency improvement due to the presence of the structured back-reflectors when compared to simple metallic flat mirrors, we defined the enhancement factor E as follows:

$$E = 100 \cdot \left(\frac{\eta_{grating}}{\eta_{flat}} - 1 \right) \tag{2}$$

with

$$\eta_{grating} = \frac{1}{2}\left[\int A_{TE}(\lambda) \cdot S(\lambda) \cdot d\lambda + \int A_{TM}(\lambda) \cdot S(\lambda) \cdot d\lambda \right] \tag{3}$$

$$\eta_{flat} = \int A_{flat}(\lambda) \cdot S(\lambda) \cdot d\lambda \tag{4}$$

where $S(\lambda)$ is the AM 1.5 solar spectrum [37].

Analogously, for the comparison between the aperiodic and periodic structures, we also define a comparative enhancement factor, given by:

$$E' = 100 \cdot \left(\frac{\eta_{grating}}{\eta_{periodic}} - 1 \right) \cdot \tag{5}$$

Although the calculation of enhancement factor should be made also with respect to randomly patterned backreflectors, this study is not easily addressable and quite challenging from the computational point of view, given the difficulty to synthesize random geometries [38]. A comparison among periodic, aperiodic and randomly textured back reflectors will be the subject of a future experimental work.

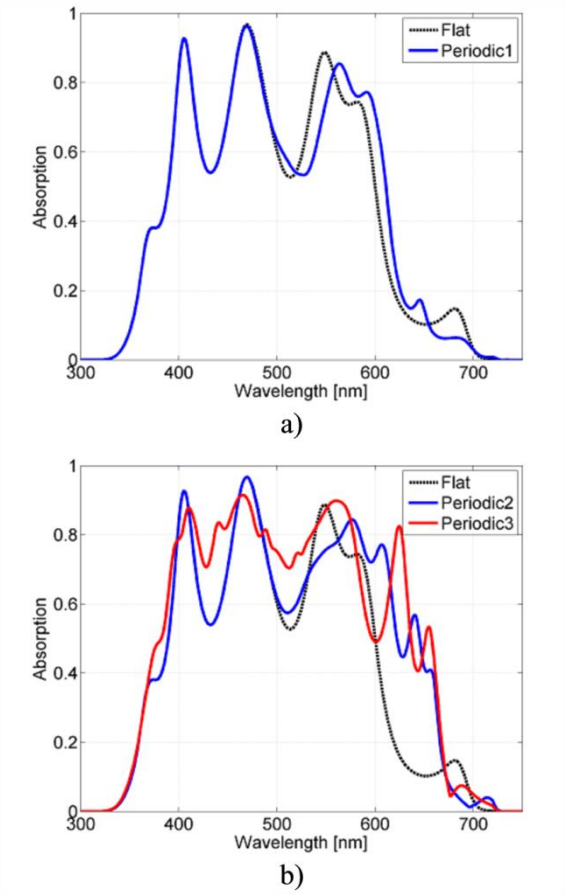

Figure 2. Absorption spectra for the optimized structures: (a) (solid blue line) spectrum pertaining to Fig. 1(b) with period *P=400nm* and *DC=0.4*; (black dotted curve) spectrum pertaining to Fig 1(a) with a flat metallic backreflector (b) spectra pertaining to Fig. 1c (blue solid curve) and Fig. 1d (red solid curve) with period *P=275nm* and *DC=0,3*; (black dotted curve) spectrum pertaining to Fig 1(a) with a flat metallic backreflector.

2.1.2 Influence of the cell geometry

In this section, we evaluate the absorption enhancements E achievable with the three different configuration of Fig. 1((b),(c) and (d)), where a periodic 1D grating of period *P* and duty cycle *DC* is used as backreflector. The duty cycle is defined as the ratio between the grating ridge width and the period. To this aim, we have carried out a parametric analysis on the light absorption evaluating *E* (defined in eq. (2)) for periods and *DC* values varying within the ranges 150-475 nm and 0.1-0.9, respectively. With reference to Fig. 1, the layers thicknesses have been chosen according to some design specifications and are fixed to be d_1=75nm, d_2=50nm, d_3=30nm, d_4=200nm, and d_5=525nm (cfr Fig. 1). Note that the layer labeled "Reflective grating" is not a physical layer, but represents the Ag back reflector extended to a thickness of d_1+d_2 in the flat case. It is only used for representing the grating thickness d_2 in all the other cases of Fig. 1 b,c, and d.

In particular, in order to correctly estimate the effective enhancement (discussed below) due to the introduction of the structured backreflector, once fixed the a-Si layer d_4=200nm, the ZnO thickness d_5 has been chosen for maximizing the absorption in a solar cell with a flat metallic mirror. At the same time, d_2 is obtained by an optimization for a periodic structure according to previous simulations [28]. The n-SiOx layer thickness (d_3) has been chosen by taking into account our previous work [13].

For the configuration of Fig. 1(b), obtained results reveal a maximum enhancement *E* of approx 3% for *P*=400nm and *DC*=0.4. We also found that for some values of *P* and *DC*, *E* becomes negative meaning that the flat mirror works even better than the structured backreflectors based on periodic nanogratings. In Fig. 2(a), we plot the absorption spectrum *A* corresponding to the maximum *E* value (blue solid line) superimposed on A_{flat} - i.e. the absorption spectrum due to a flat silver mirror (black dotted line).

As evident up to wavelengths shorter than ~500 nm, the absorption spectra basically overlap each-other, meaning that photons are mainly absorbed before they reach the bottom of the cell and no significant light interaction occurs with the backreflector. In the same range, the Fabry-Perot effect due to the thick ZnO top layer gives its maximum contribution. Although one would expect that the excitation of guided photonic modes in the a-Si planar layer and/or plasmonic modes at the semiconductor-metal interface (only in the TM case) would produce absorption peaks superimposed to the Fabry-Perot envelope [21] here we found that the presence of the uniform n-SiOx layer strongly frustrate the optical field connected with these resonant modes, especially within the active region of the cell. This is the main reason for the very weak absorption enhancement observed in case of structured back-reflector even at longer wavelengths.

To overcome this limitation, we consider the structure of Fig. 1(c) where the periodic patterning is imposed also within the n-SiO_x layer. In Fig. 2(b), we plot the absorption spectra only for the optimum case (maximum absorption enhancement) achieved for period *P*=275nm and *DC*=0.3 and corresponding to an enhancement *E*=14% (blue line).

In this case it is evident that the Fabry-Perot envelope for wavelengths longer than 500 nm is interrupted by few absorption peaks generated by the excitation of both guided photonic modes and plasmonic modes. It should be noted that the plasmonic contribution, being strongly localized at the interface between silver and n-SiOx, provides an absorption enhancement lower than the photonic counterpart given by guided modes along the silicon layer. Although it is small, this contribution is not entirely negligible, since the layer of n-SiOx is very thin (d_3=30 nm), and then the tail of the e.m. field reaches also the silicon region.

A significant improvement can be obtained with the structure of Fig. 1(d); in fact a maximum enhancement of about 22% can be achieved for *P*=275 nm and for *DC*=0.3. The absorption spectrum of the optimized structure is plotted in Fig. 2(b) as red line. In this latter case, the introduction of a grating on the top of the structure basically breaks the Fabry-Perot effect for wavelengths shorter than 500 nm (i.e. in the absorbing spectral range where the metallic backreflectors do not give a significant contribution), and now several absorption peaks can be distinguished, which are responsible for the absorption enhancing. In practice, the top grating acts also as a grating coupler for guiding the modes inside the a-Si region.

In our analysis, when comparing the structures of Fig. 1, we keep constant the value of d_4 (the distance between the nSiOx buffer layer and the ZnO top contact layer); this implies that the structure of Fig. 1c, has intrinsically a larger silicon volume. However, despite the smaller absorption volume which generally prejudices the absorption enhancement, the last configuration outperforms the previous one, providing a real advantage in terms of light trapping efficiency. This case, where the silicon layers are deposited on pre-textured substrates (fig. 1(d)), is also the most interesting and direct approach, easily scalable to the large areas required in thin film PV module production [33].

For the configuration of Fig. 1(d), in the rest of the document, we carried out a comparative study on the light trapping efficiency in case deterministic aperiodic nanogratings are employed as structured back-reflectors.

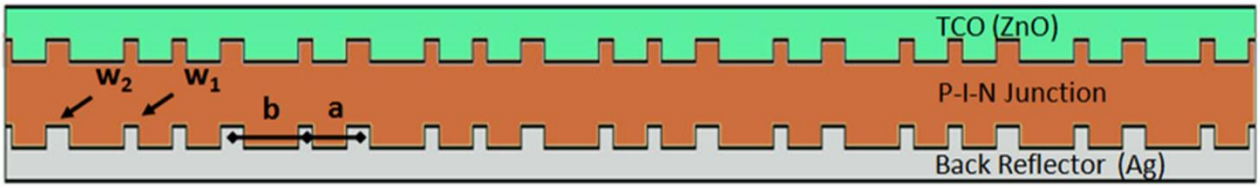

Figure 3. Schematic of the solar cell structure based on an aperiodic Fibonacci-like backreflector. The grating element widths (w_1 and w_2) and the distances between them (*a* and *b*) are indicated.

2.2 Fibonacci-like backreflector

The cell based on the Fibonacci-like grating backreflector is schematically shown in Fig. 3. In this configuration the grating ridges are separated each-other by two different distances *a* and *b* alternated by

iteratively applying the substitution rules $a \rightarrow ab$ and $b \rightarrow a$, according to the Fibonacci sequence [29]. Evidently, this substitution process can be iterated ad infinitum, yielding to an infinite sequence and thus a global aperiodic structure. It is also clear that is impossible to simulate a structure composed of an unlimited number of elements. For this reason, it is necessary to truncate the Fibonacci sequence at a number of element chosen as good compromise between valid results and computational resources/time.

The truncated structure constitutes the supercell that is replicated in space by applying the periodic boundary conditions, leading thus to a periodic structure with a aperiodic supercell. Specifically, we have considered in our numerical study, a sequence truncated at the 7th-order corresponding to a supercell of 21 elements/distances (*abaababaabaababaababa,* considering the "*b*" element as the zero order). The ratio between the two distances is chosen to be the golden mean $\tau = b/a = (1+\sqrt{5})/2 = 1.618$. Note that $\tau = 1$ identifies the periodic case.[39] In order to make straightforward the comparison, the average period of the Fibonacci grating P_{ave} has been defined as the ratio between the supercell length *L* and the number of grating ridges, i.e. $P_{ave} = L/(n_a + n_b)$ where n_a and n_b are the number of the "*a*" and "*b*" elements of the sequence, respectively. Moreover, we have defined two ridge widths $w_1 = DC. \times a$ and $w_2 = DC \times b$ in such a way to have - in analogy to the periodic case - an uniform silicon or metal layer for $DC = 0$ or 1, respectively. In other words, we have set the grating parameters to obtain, in both the periodic and aperiodic cases, *exactly* the same area of silicon (or silver) within the grating for each combination of average period P_{ave} and *DC*.

Similarly to the previous analysis, we have calculated the light absorption for equivalent periods and *DC* within the range 150-475 nm and 0.1-0.9, respectively. To summarize the results and better highlight the differences with respect to the periodic case, we show in Fig 4(a) a map of the comparative enhancement factor *E'*. Although *E'* values up to 3.4% have been found against a maximum decrease of 1.7%, it is evident that Fibonacci backreflector does not introduce a significant light trapping enhancement when compared with the periodic counterpart. As matter of fact, a maximum enhancement *E* value for the Fibonacci like backreflector is found to be 22.4% (very close to 21.7% found in the periodic case) for P_{ave}=275nm and *DC*=0.3. In Fig. 4(b) the absorption spectra for the optimized aperiodic (red line) structure is plotted together with the periodic (blue line) counterpart with the same period *P*=275nm and *DC*=0.3. The spectra are superimposed on the AM 1.5 solar spectrum normalized to its maximum (magenta line) and on the absorption spectrum A_{flat} obtained with a flat silver mirror (black dotted line).

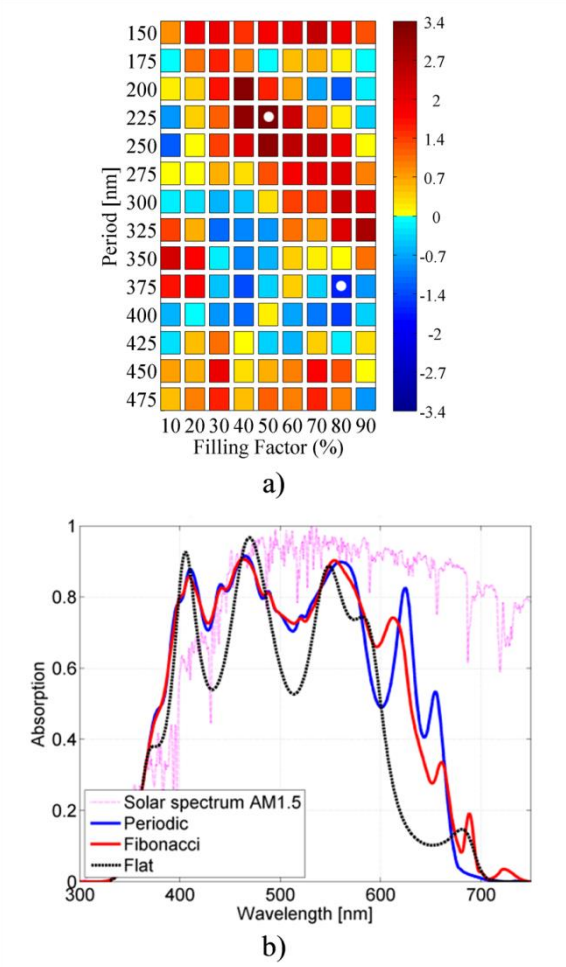

Figure 4. (a) Map of the absorption enhancement *E'* for the configuration of Fig. 1d; the maximum (3.4) and minimum (-1.7) values are marked with white dots. (b) absorption spectra for the optimized periodic (*P*=275nm - *DC*=0.3, blue solid lines) and quasi-periodic (P_{ave}=275nm - *DC*=0.3, red solid lines) structures. The AM 1.5 solar spectrum (magenta-dotted) and the absorption spectrum of the solar cell with a silver mirror as backreflector (black-dotted) are also shown.

In principle, according to ref.28, it would be expected that, in the periodic case, a lower number of absorption peaks would appear in the spectrum because of the excitation of a lower number of photonic/plasmonic modes. This seems to occur only for wavelengths around 700 nm, just at the band edge of the absorption spectrum.

2.2.1 Influence of the amorphous Si optical properties

The results discussed so far refer to the experimental a-Si model. Fig. 5 shows the real (dotted blue line) and the imaginary (dotted red line) part of the a-Si refractive index as a function of the wavelength, the latter approaching zero around 700 nm. Obviously when the imaginary part (extinction coefficient) *k*=0 no light absorption inside the active region can exist. It is thus clear that the steep falling edge of *A* is essentially due to the falling edge of the experimentally evaluated *k* used so far in our simulations.

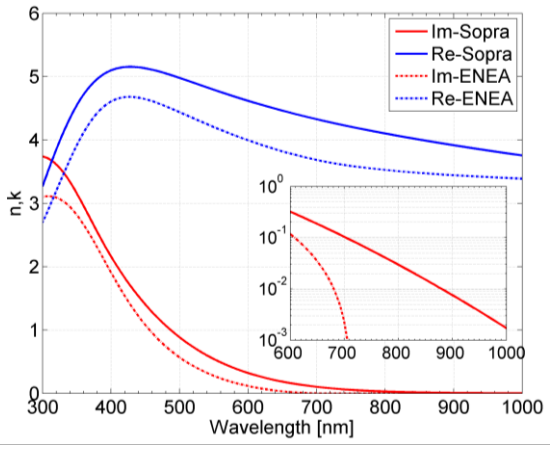

Figure 5. Real and imaginary parts of the a-Si refractive indexes: (dotted lines) ENEA: experimental (measured) model; (solid lines) SOPRA: numerical model. The inset shows a zoomed-in detail of the imaginary parts in log scale.

The role of the active region optical properties on the light trapping in presence of a structured backreflectors has been investigated by considering also a tabulated alternative a-Si model [40] in which the real part *n* is slightly larger and *k* decays more slowly at longer wavelengths (see solid lines in Fig. 5, and the inset where the extinction coefficient are compared in a log scale). This comparison is essentially performed for evaluation purposes, as such optical properties correspond to a-Si:H with low hydrogen concentration, whose use in real solar cells is hampered by the unsuitable electrical properties.

Anyway, with this new a-Si model, thanks to the extinction coefficient profile extending to longer wavelengths (as clearly shown the inset of Fig. 5), we expect to have a greater contribution of the structured backreflector since the resonant effects occurring at wavelengths larger than 700 nm can give a significant effect to the absorption and eventually increase the differences between periodic and aperiodic patterns.

We have thus calculated again the absorption for both the periodic and aperiodic backreflector for the structure of Fig. 1(d) with the new a-Si refractive index model taken from ref.40. In Fig. 6(a), we plot the comparative enhancement factor *E'*, where it is evident that this time the aperiodic backreflector globally outperforms the periodic one for most of the equivalent periods and duty cycles here considered. An enhancement factor *E'* up to 5% was obtained against a maximum decrease of only 0.7%. The maximum absorption enhancement *E* obtained for the Fibonacci is 26% (P_{ave}=300 nm, *DC*=0.3) compared to 22% (P_{ave}=275 nm, *DC*=0.3) achievable with the periodic counterpart. The corresponding absorption spectra for the two *optimized* structures are plotted in Fig. 6(b), where the red and blue lines refer to the Fibonacci and periodic grating respectively; as a reference, we also plot in the same figure the AM 1.5 solar spectrum normalized to its maximum (magenta line) and on the absorption spectrum A_{flat} obtained with a flat silver mirror (black dotted line). In this case the absorption spectrum relative to the Fibonacci backreflector clearly exhibits a larger number of absorption peaks reflecting the fact that a larger number of photonic/plasmonic modes have been excited inside the structure (especially in the long wavelength range).

It results clear from the above results, that only the concurrent optimization of all degree of freedom (including material properties and backreflector design) of the final device, permits to have a real benefit in terms of final performances of the cell, justifying the higher fabrication complexity when structured backreflectors are employed. In particular the real advantage offered by the aperiodic nanograting (which allows to allocate a larger number of resonances in the high wavelength range), can be exploited only by selecting the material with appropriate optical properties.

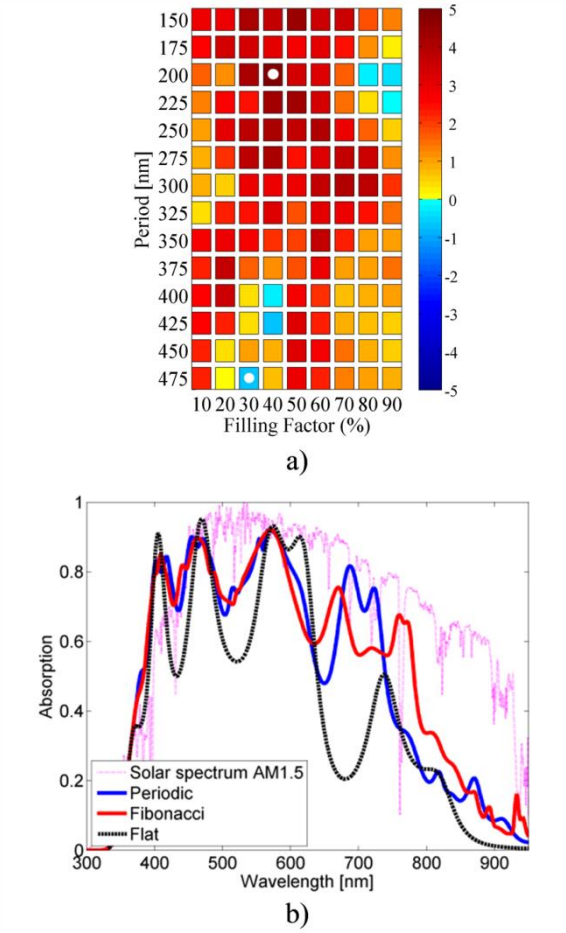

Figure 6. (a) Map of the absorption enhancement *E'* for the cell configuration of Fig. 1d calculated considering the SOPRA Silicon refractive index model; the maximum (5) and minimum (-0.7) values are marked with white dots. (b) absorption spectra for the optimized periodic (*P*=300nm - *DC*=0.3, blue solid lines) and quasi-periodic (P_{ave}=275nm - *DC*=0.3, red solid lines) structures. The AM 1.5 solar spectrum (magenta-dotted) and the absorption spectrum of the solar cell with a silver mirror as backreflector (black-dotted) are also shown.

2.2.2 Remarks on the supercell approximation and the scale ratio τ

As previously mentioned, the results presented in this work pertain to a 21 elements supercell obtained by truncating the Fibonacci grating to the 7th order. Our choice is mostly related to computational affordability considerations, as mentioned in previous sections. We wish to stress that our findings are representative of a genuine aperiodic phenomenology; in fact we carried out a study on the absorption spectra dependence on the Fibonacci sequence order. We gradually increased the supercell size up to the maximum affordable value (10th order corresponding to 89 grating elements) and observed the presence of consistently similar spectral features. In practice the absorption spectra relative to orders from 6 to 10 essentially overlap with each other meaning that the 7th order can be considered a valid approximation of the *global* aperiodic structure.

In principle, we could exploit the additional degree of freedom represented by the scale ratio τ in the Fibonacci sequence to further maximize the light absorption. To evaluate this possibility, we have calculated the absorption enhancement *E* as function of τ varying in the range [1-5] and not integer multiple of the 1.618. We have found that the maximum *E* is just achievable for values of τ=1.618.

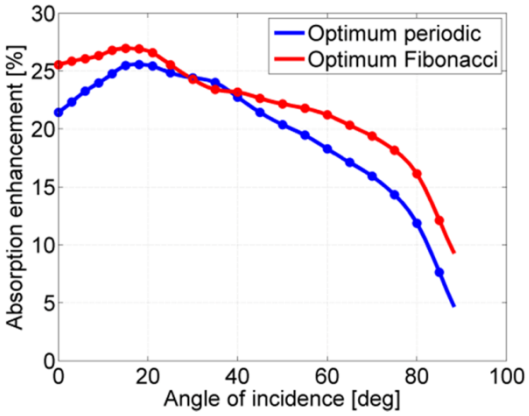

Figure 7. Absorption enhancement versus incident angle for optimized periodic (*P*=300nm - *DC*=0.3, blue solid lines) and quasi-periodic (P_{ave}=275nm - *DC*=0.3, red solid lines) structures pertaining to Fig. 1d.

2.3 Influence of the incidence angle

The above analysis has been restricted to the case of solar radiation impinging on the cell as a normally incident plane wave. This is clearly an approximation because of the almost isotropic behavior of the solar irradiance[41]. To make our analysis more general and close to the real application, we have also studied the absorption dependence on the incident angle ϑ for the optimized structures with the a-Si model in ref.40; in Fig. 7, we plot the *E* values for both Fibonacci (red line) and periodic (blue line) cases as function of the incidence angle in the range 0-85 degrees, chosen to cover a large amount of the solar radiation diagram [41,42]. The enhancement curves for both the configurations have a similar trend with an absorption enhancing ranging from about 10 to 27%.

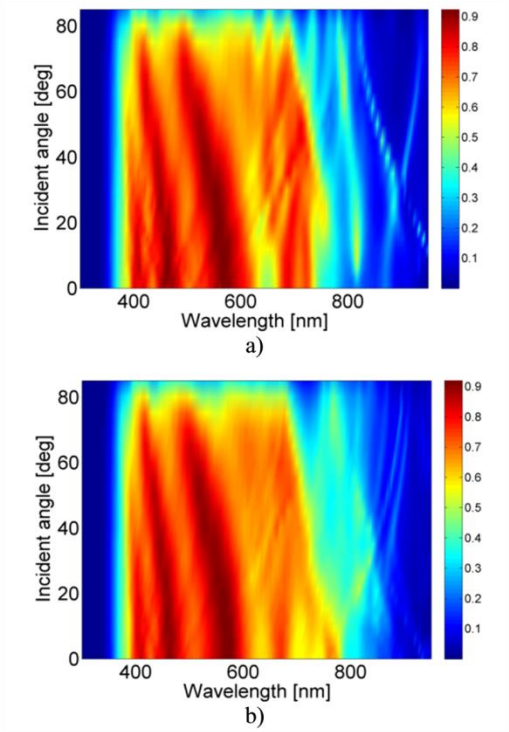

Figure 8. Pseudo color plot of the absorption of periodic (a) and Fibonacci (b) configuration of Fig. 1d as function of the incident angle θ evaluated in range [0-85]°.

In general the results demonstrate that the absorption enhancement achievable with metallic gratings is not so much affected by the incident angle. However, the Fibonacci backreflector averagely guarantees better performances over the whole incidence angle range, providing a slightly stronger enhancement of about 5% for angle less than 20 deg and for angles greater than 45 deg. To provide a better explanation and interpretation of these results, we report in Fig. 8 the contour plot of the absorption *A* for both the periodic (a) and aperiodic case (b), respectively. First of all, it can be easily observed that the absorption peaks split for $\vartheta \neq 0$ because of the resonant modes degeneracy that breaks the symmetry of scattered wavevectors [43]. The resonance splitting is beneficial for small incidence angle, thus increasing the total absorption enhancement of ~3% for θ close to 10 deg. For $\vartheta > 20$ deg. instead, the split resonant peaks tend to decrease their intensity, thus causing a decrease of *E*. Similar considerations hold also for the Fibonacci grating; however, in this latter case, the higher number of excited resonances is responsible for the more isotropic behavior (particularly evident in the range 700-800 nm).

2.4 Experimental Section

In order to verify the feasibility of different nanopatterning strategies proposed in the previous sections, the Focused ion beam (FIB) has been used to realize array of micro-nanochannels both on n-SiOx:H film, used as the n-layer of the junction, and on ZnO layers, used as the front electrode of the device.
In general, when energetic ions hit the surface of the target, a variety of ion–target interactions, including swelling, sputtering, redeposition, implantation, backscattering and nuclear reaction, can occur. In recent years, many approaches and research results have indicated that redeposition of sputtered target atoms, after the striking of the ion beam onto the surface, is the most serious problem in fabricating micro and nano devices. This phenomenon creates a V-shape of the milled structures. This typical profile is due to the ion beam which has a Gaussian current density distribution and the center of the groove has a higher yield than the edge [44-47]. The redeposition must be minimized to have perfectly vertical sidewalls and to guarantee low-loss propagation, in the field of photonic applications by adopting suitable milling strategy [48]. Fabricating submicron trenches with perfectly vertical sidewalls by FIB milling is challenging [44,49,50]. A suitable milling strategy must to be adopted for reducing the effect of material redeposition, like choosing the appropriate dwell time (time interval that the beam remains on one milling point before moving to next one), single-pass or multi-pass milling of individual pattern elements (number of times that pixel array is exposed), the definition of beam size (varying the beam current), and consequently the dose (total ion current applied in a precise time) applied to the target area.

2.4.1 Nanopatterning on n-SiOx:H

In the first part of experimental activity starting from the results presented in the report of the last year, phosphorous-doped SiO_x layers (90-nm-thick) have been deposited by plasma enhanced chemical vapor deposition (PECVD) at standard frequency (13.56 MHz) on Corning Eagle glass using carbon dioxide (CO_2), silane (SiH_4), hydrogen (H_2), and phosphine (PH_3). One such film was inserted in the vacuum chamber of the focused ion beam (Quanta 200 3D FEI instrument) and evacuated to a pressure of 10^{-6} mbar. Nanochannel dimensions, width 140nm, length 5μm and depth 80nm, suitable for light trapping applications, have been considered. One rectangular channel was milled in order to understand the dependence of FIB parameters on the milled structure. Two nanochannels with a separation of 140nm were milled by FIB for understanding the effect of redeposition on the separation between two milled trenches, whose thickness could modify subsequently the light trapping in thin film solar cell. However, the realized patterns show an amount of redeposition (called R in fig. 11a), around 10 nm. This value is too low to involve some change in the diffraction grating. A typical image of two milled trenches is reported in the Fig. 9.

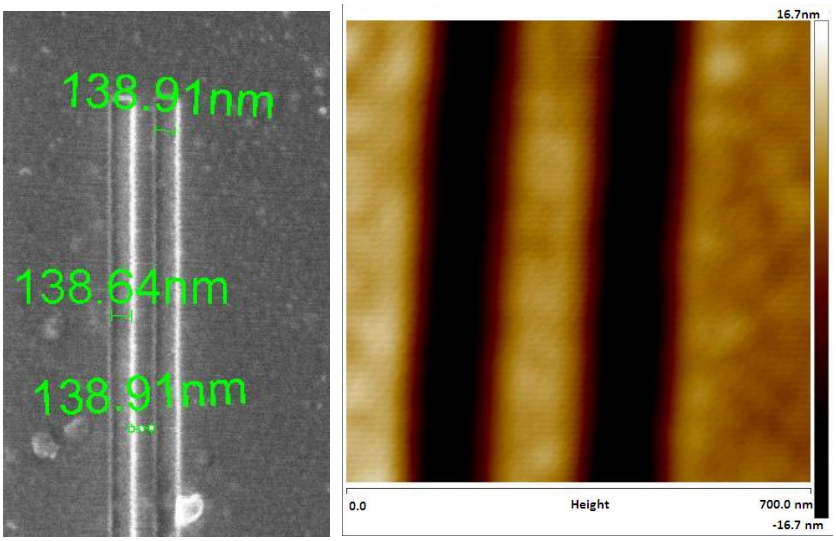

(a) (b)

Figure 9. Typical (a) FIB image and (b) AFM image of two milled nanochannels on n-SiOx:H.

The acceleration voltage is fixed at 30keV while the ion beam current, that controls the dimension of the ion beam, is varied in the range from 1pA to 50 pA. The profiles of milled trenches were analyzed by atomic force microscope (AFM) using Nanoscope IV Dimension digital instruments Veeco operating in tapping mode with a small tip radius (r ~ 10 nm). The aim is to control the shape of the right nanochannel which must have a box-shape, with vertical sidewalls. The simulated sputtering yield is performed using Monte Carlo simulations, using the TRIM 2012 (transport of ions in matter) program [51]. It simulates ion bombardment defining the target, the ion elements, incidence energy, incidence angle, and the number of incoming ions, calculating the sputtering yield for each atom present in the film. For calculating these values, TRIM needs the concentration of elemental atoms present in the compound layer. The material concentration in n-SiOx:H film has been evaluated through Rutherford Backscattering Spectrometry (RBS), by using a 2.0 MeV He+ beam [52]. TRIM sputtering yield depends on surface binding energies, surface structure and chemistry and it does not considering the channeling effects [53]. Then experimental sputtering yield is calculated and compared with TRIM results.

2.4.2 Time-dependent milling on n-SiOx:H

Since the thickness of the n-SiOx:H thin film is 90 nm (from profilometer analysis), it necessary to mill the thin film without reaching the glass for light trapping applications. Then it was important to know the time required to mill at least 80 nm depth for obtaining the settled nanochannel. An end point monitor (EPM) graph in the FIB machine serves the purpose. It detects the absorbed sample current during the milling process. The absorbed current generated while milling is material dependent and can be used to identify different materials in a multi-layered structure [54]. A typical EPM graph is reported in fig. 10, obtained for 1nA ion beam current. The arrow indicates the time, 7sec, when n-SiOx:H film is completely milled at 1nA and ion beam starts to mill the glass. In fact at that point the absorbed sample current changes. In the following experiments, by analyzing the EPM graph, a correct milling time is fixed for each applied current to obtain the depth of 80nm.

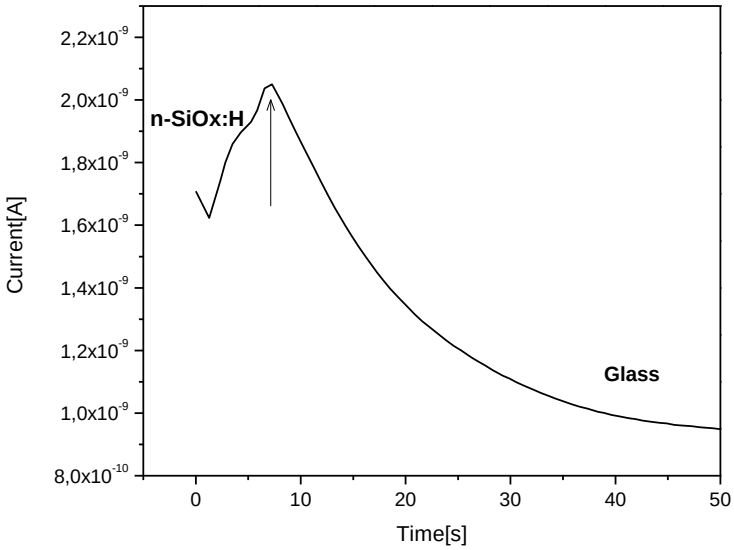

Figure 10. EPM data are recorded while FIB is milling the n-SiOx:H film using 1nA ion beam current. The arrow shows the time when the film is completely milled and FIB starts to mill the glass

2.4.3 Redeposition and its Dependence of FIB milling parameters on n-SiOx:H

When ion beam strikes the target area, material will be milled, but sputtered target material can be redeposited onto the sidewalls of the nanochannel by modifying the shape. The redeposition problem can be lowered by adopting different scanning strategy for obtaining vertical sidewalls. The FIB milling parameters which influence the ion beam impact on surface and consequently the redeposition are: milling direction, scan routine, magnification, dwell time, number of loops (number of times that pixel array is exposed) and total ion dose, that is total ion current (ion current x time) applied to the target area.

2.4.3.1 Milling direction and scan routine

The milling direction and scan routine have important roles in the redeposition of milled materials on the sidewalls.[45] The rectangular trench can be milled in different direction: right to left, left to right, bottom to top and top to bottom. Furthermore the scan routine can be serial or parallel [55]. In the serial scanning, the ion beam scans the sample and the beam does not totally switch off from one pixel to the closest one, then this scanning procedure results in more redeposition. In the parallel scan where the ion beam does not step over the milled structure, straight sidewalls are achieved. Then by fixing scan routine as the parallel scan, the milling direction is changed. The milled profiles of the nanochannels are shown in Fig. 11 by using the same ion current at 50pA, with parallel scanning, but changing the milling direction. The milling from “right to left” (Fig.11a) results in more redeposition onto the sidewalls with respect to “bottom to top” direction (Fig.11b). Also the bottom of the nanochannel is more flat when “bottom to top” is used. The values of depth, D, width, W, and surface redeposition, R, evaluated from original surface, the line at 0 value (defined as reported by Tseng et al. [56] and drawn in the figure 11a), are quite similar but the shapes are different. Then “bottom to top” direction milling and parallel scanning have been chosen for the following patterning.

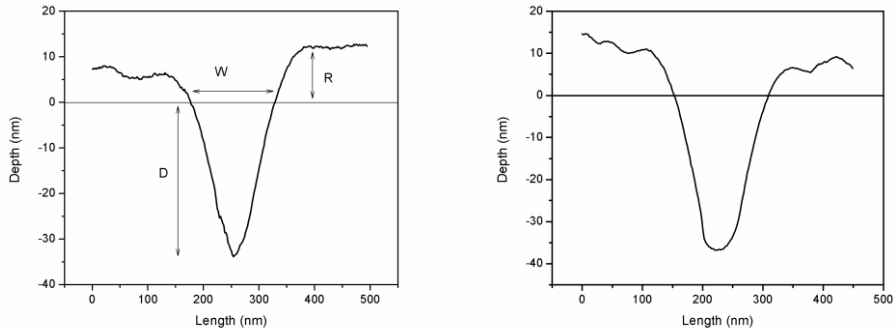

(a) (b)

Figure 11. AFM images of the milled trenches with different milling direction. In (a), depth, D, width, W, and surface redeposition, R, (typically around 10nm) are drawn starting from the original surface at 0 value. (a) Milling direction "right to left" (D=33nm, W=152nm) and (b) "bottom to top" (D=37nm,W=156nm)

2.4.3.2 Magnification

The magnification determines the field of view for the milling. It defines the maximum area that can be scanned by the ion beam at once. The AFM profiles of the milled trenches are reported in Fig. 12, to study the dependence of magnification on the shape and on the redeposited material, at fixed dose of $9x10^{16}$ ions/cm^2.

The higher magnification results in a more defined shape (fig.12a) where the redeposited material is less both onto the surface and to the sidewalls. It is also evident that the depth of milled trench at lower magnification (fig. 12b) is less than that at higher magnification, due to the low resolution of the scanned area. The magnification has been fixed to 19716 times resulting in a writing field of about 15x12μm^2.

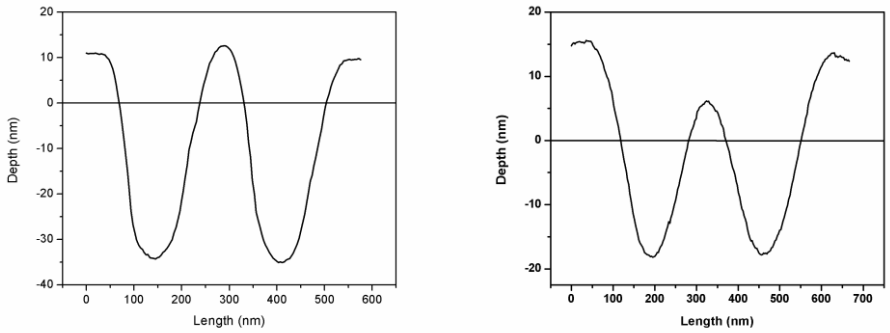

(a) (b)

Figure 12. Two boxes milled by fixed dose of $9x10^{16}$ ions/cm^2 with a magnification of (a) 19716x (D= 34nm,W=168nm) and (b) 8308x (D=18nm,W=178nm)

2.4.3.3 Dependence of dwell time

The redeposition can be influenced by changing not only the scan direction and magnification, but also modifying the dwell time [57]. The dependence of the dwell time on the sidewall redeposition was studied by keeping the total dose, applied to each box, constant. In Fig. 13 the nanochannels have been milled at 1pA and by changing the dwell time. The nanochannels show a symmetric profile at dwell time of 1μs. The use of excessively large (greater than 1μs) or small (smaller than 1μs) dwell times lead to significant redeposition and asymmetric feature shapes. Then the dwell time in the following milling tests was fixed at 1 μs.

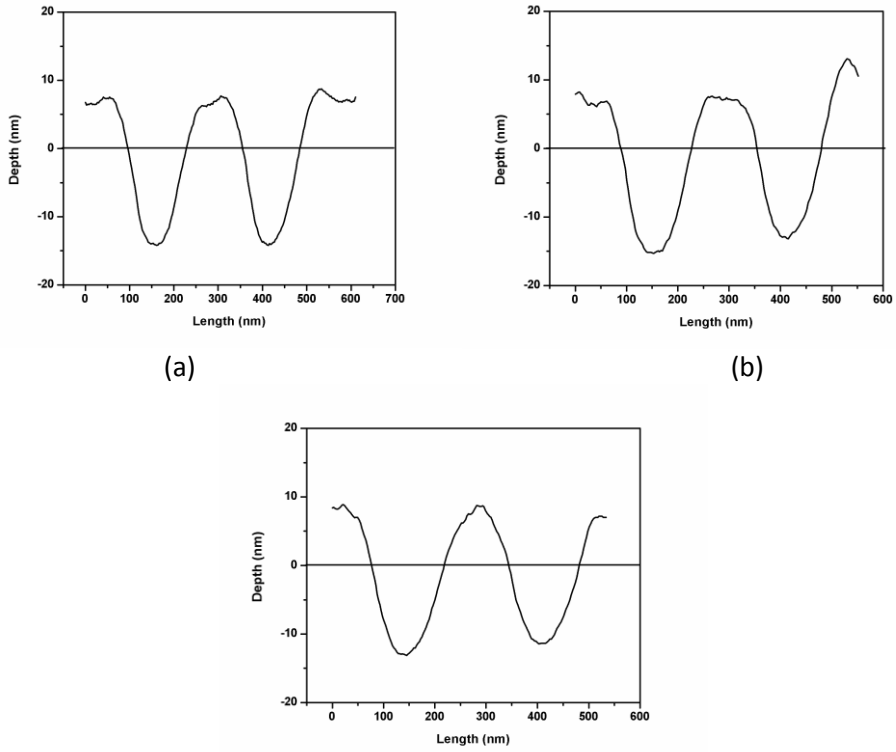

Figure 13. AFM profiles of the milled trenches at fixed current, 1pA, and different dwell times (a) 1μs (D=14nm, W=133nm) (b) 500ns (D=13-15nm, W=138nm) and (c) 100 ns (D=11-13nm, W=142nm)

2.4.3.4 Dependence of number of loops

Another parameter to be considered is the number of loops (or passes of the beam necessary to make the mill run). Changing dwell time in a scan pattern, leads to a change in required loop number to achieve similar milling depths. If dwell time of 1ms is used, the number of passes is 1 and the mill is named as "single-pass" milling. When the dwell time decreases, the number of loops proportionally increases, keeping the product constant. When the number of loops increases the milling is named as "multi-pass". This strategy prevents redeposition as any redeposited material in a pattern will be removed in the subsequent pass. For controlling the dependence of the number of loops on the trench shape, the dwell time and depth are fixed while the ion beam current is changed.

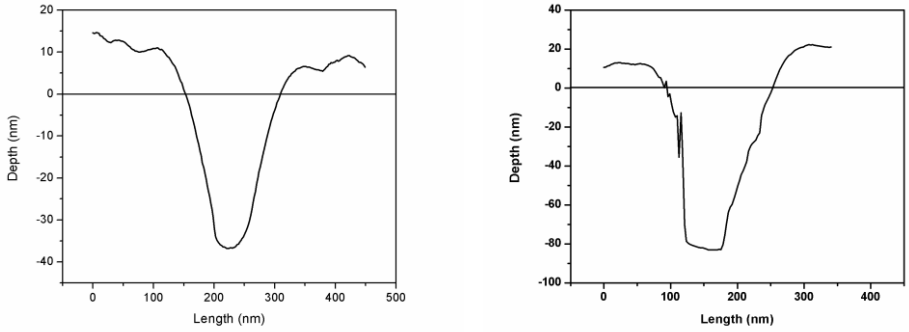

Figure 14. AFM profile of the milled trenches at (a) Ion current is 50pA, dose is $9x10^{16}$ ions/cm^2, dwell time is 1μs and passes are 271 (D= 36nm, W=158nm), (b) Ion current is 1pA, dose is $3x10^{17}$ ions/cm^2 , dwell time is 1μs and passes are 6125 (D=83nm, W=158nm)

Fig. 14a and 14b show the milled nanochannels at 50pA and 1pA, respectively, with the same dwell time, 1µs, but with different number of loops. Although the milling time is same (evaluated from the EPM graph), for both samples, to reach 80 nm, the depth is different because of redeposition that is larger for few number (fig. 14a) respect to high number of passes (fig.6b). The depth, D, of the milled trenches for large number of loops (fig. 14b) is equal to settled one, at 80 nm.

2.4.3.5 Dependence of total ion dose on milling

Furthermore the cross-sectional profile of the milled channels changes significantly as a function of ion dose. The ion dose was varied by milling the trenches at a fixed beam current for different times. Different ion beam currents have been used for milling the trenches, and the results obtained at 1pA (the minimum ion current), and 50pA are presented here. When the ion current is more than 50pA, the V-shape profile is more pronounced and it is very hard to reduce it. The AFM images of the trenches after milling with different dose are shown in Fig.15. When the dose is high, the V-shape is more pronounced (Fig. 15a), whereas the channel start to improve its profile by reducing the dose (Fig. 15b). At lower ion doses (Fig. 15c and 15d) the milled channels have quite similar box-shape. But when the dose is too low (Fig. 15d), the milling is slow and then it is not possible to obtain the settled depth. Typical 3D AFM images of V-shape and box-shape are shown in Fig. 16.

From all these experimental data, when the dose is in between $3x10^{17}$ ions/cm^2 and $5x10^{17}$ ions/cm^2, different shapes are observed for a trench of fixed depth (fig. 5a and 5c respectively). If the dose is lower than $3x10^{17}$ ions/cm^2 the quantity of ions is too low for obtaining a regular shape with a defined depth (fig. 15b and fig. 15d). The better dose, to obtain the right depth and a quite regular box shape, is $3x10^{17}$ ions/cm^2, at 1 pA and dwell time 1µs. In the next sections sputtering yield for the film is calculated both theoretically and experimentally.

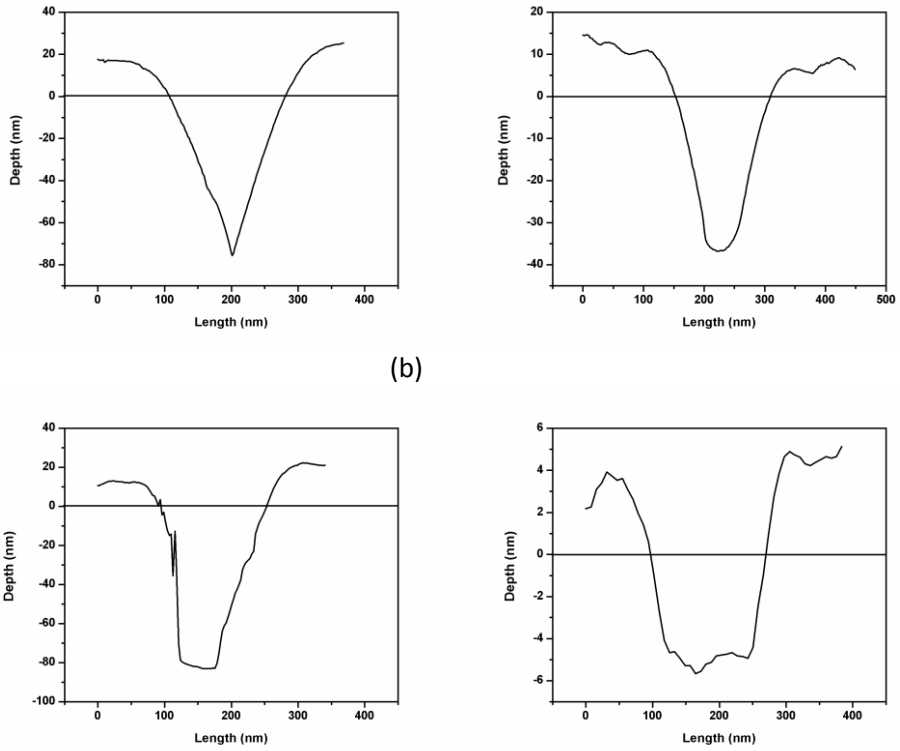

Figure 15. AFM profiles of the milled trenches at 50pA with doses a) $5x10^{17}$ ions/cm^2 (D=75nm, W=174nm) and b) $9x10^{16}$ ions/cm^2 (D=37nm,W=156nm); and at 1pA with doses (c) $3x10^{17}$ ions/cm^2 (D=83nm, W=158nm) and (d) $5x10^{16}$ ions/cm^2 (D=5nm, W=172nm)

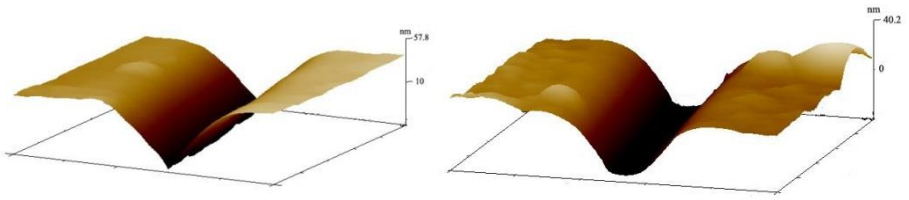

(a) (b)

Figure 16. Typical 3D AFM images of V-shape (a) and box-shape (b)

2.4.4 Sputtering yield of n-SiOx:H

Simulation of physical and chemical phenomena induced by ion beam is essential to manipulate and fabricate micro/nano shapes [46]. An important parameter is the sputtering yield, Y, defined as the number of ejected particles per incident ion. It depends on ion energy, ion beam current, dose, ion beam angular incident, mass, crystal orientation, substrate nature. It is possible to evaluate the value both experimentally and theoretically.

2.4.4.1 Prediction of sputtering yield by TRIM

The theoretical prediction of the material removal rate (sputtering yield) of layer has been evaluated using the FIB with normal incident of 30keV Ga+ ions on the sample surface. For the simulation studies, 10000 Ga+ ions, impinging on the layer surface, are considered to minimize statistical error in the simulation. TRIM uses three key calculation parameters for the target material. They are the lattice displacement energy, surface binding energy and lattice binding energy, used subsequently to calculate the sputtering yield.

Table I. The parameter (in eV) extracted from TRIM simulation of the n-SiO_x:H compound

Composition n-SiO_x:H	Lattice binding energy	Surface binding energy	Displacement energy
Si (74%)	2	4.7	15
O (22%)	3	2.0	28
H (3%)	3	2.0	10
P (1%)	3	3.3	25

By using the atomic content estimated by RBS, n-SiO_x:H density ($\rho_{l\,=}$ 2.055 g/cm^3), lattice binding, surface binding and displacement energy (Table I) can be estimated using TRIM program. TRIM uses these parameters to calculate the sputtering yield of each atom which composes the n-SiO_x:H layer (Table II). The simulation gives a prediction for the total sputtering yield ($Y_{Si+O+H+P}$= 2.74). In the successive subsection the experimental sputtering yields are shown and compared with this result.

Table II. Sputtering yield of different elements in n-SiO_x:H compound calculated by TRIM

Atom type	Sputter yield (atoms/ion)
Si	1.74
O	0.91
H	0.06
P	0.03

2.4.4.2 Experimental sputtering yield for different beam currents and ion dose

There are two ways to find experimental sputtering yield [58]. The former, Y_v, is the milled volume removed per unit charge for singly charged ions, which is calculated by

Y_v = milled Volume/ion charge = μm^3/nC = μm^3/ (ion beam current (nA) x time (sec)) (1)

The latter, Y, is defined as atoms ejected per incident ion:
Y =number of atoms removed from incident surface (N_t) / incident ions (N_i) (2)
In Fig. 17 the sputtering yield is calculated from the slopes of linear fit (as reported in eq. 1) for two different ion currents. It is evident that the milled volume increases linearly with the ion dose within the ion current value. The sputtering yield, calculated from the slopes, 0.195 μm^3/nC at 50pA and 0.162 μm^3/nC at 1pA, shows that it is directly proportional to the beam current in the dose range of the present study. Considering that 1000 μm^3/ nC ~ 10000 atoms/ion, these values become 1.95 atoms/ion at 50pA and 1.62 atoms/ion at 1pA.

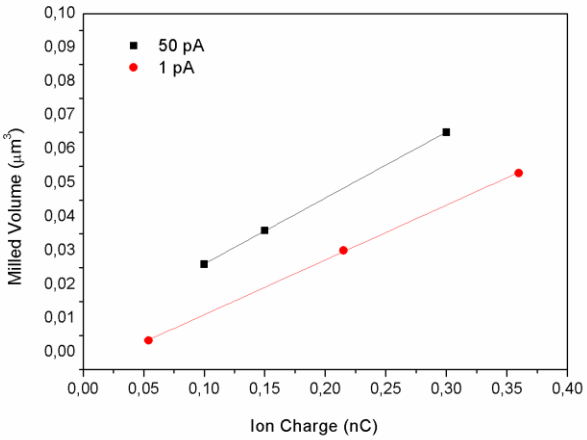

Figure 17. Milled volume dependence from the ion charge for different currents (1pA and 50pA). Straight lines represent the best fit

The other method to determine the sputtering yield is to use the equation (2) where total number of removed atoms, N_t, is given by the following equation [58]:
$N_t = W_r/W_l \times N_l = ((V_l \times \rho_l)/W_l) \times N_l$ (3)
where W_r is the weight of removed volume (measured by AFM) ; W_l is the molecular weight of layer, N_l is number of atoms in the layer, which is 4 for n-SiO_x:H; V_l is the volume of the layer removed by FIB; ρ_l is the density of the layer, which is about 2.055 g cm^{-3} as calculated by TRIM.
Considering that 1nC/μm^2 =6.25x10^{17} Ga^+ ion/cm^2 and 1 atom= 1.66x10^{-24} mol and 1000 μm^3/ nC ~ 10000 atoms/ion, the sputtering yield for N_i=9x10^{16} ions/cm^2 (with a beam current of 50pA) is 2.78 atoms/ion while for N_i=3x10^{17} ions/cm^2. (with a beam current of 1pA) is 1.6 atoms/ion. Since the redeposition is correlated to sputtering yield, when 9x10^{16} ions/cm^2 is applied a large number of sputtered atoms are generated and that results in higher redeposition, as it is also evident from the shape shown in fig. 15b. The redeposition is less when 3x10^{17} ions/cm^2 is applied because of smaller value of Y, less sputtered atoms are produced and then less atoms are redeposited onto the sidewalls resulting in a nanochannel having quite similar to a box-shape (fig.15c). When eq. (1) is used to calculate the sputtering yield, different values of Y_v are obtained at the same ion dose, if different currents are applied. While, using eq. (2), the value of sputtering yield is unique if the ion dose is settled. The sputtering yield calculated by TRIM can be compared to experimental sputtering yield obtained by eq. (2), finding that the TRIM value is similar to that calculated at 9x10^{16} ions/cm^2 dose. From these results, it is evident that the values of sputtering yield, calculated both theoretically and experimentally, are not easily comparable because n-SiO_x:H is a compound target and other theories are necessary to calculate the theoretical sputtering yield by incorporating the implantation and out-diffusion of the primary ion species, as well as other parameters as well reported in literature [59,60]. The actual effect of sputtering yield on the shape of the milled nanochannel is not predictable only with TRIM data. These values can foresee only if there will be more or less redeposition in the nanochannel milled with a precise ion dose. It could be more interesting, in a future work, before starting the milling, to have other information to model the shape of the milled structure,

using a code capable of simulating the surface topography in 2D and 3D space including angle dependent sputtering and redeposition [61,62].

2.4.5 Nanopatterning of ZnO layer

In the final part of the experimental activity ZnO layers have been nanopatterned by following the interesting results obtained by numerical simulations for the configuration shown in Fig 1d. It is important to note that the FIB nanopatterning on this configuration should not have any impact in the fabrication process of the cell because the milling does not interrupt the manufacturing process of the active part of the device. The nanopatterned area is equal to 0.5 cm^2. This area is considered to be a large region for the FIB technology and its patterning should take very long times that obviously depend on the geometric parameters defined for the realization of the channels. Then, in this preliminary step, a short time has been chosen to perform some test in order to verify only the feasibility of the whole process. This has been possible not using the geometrical parameters suggested by the theoretical predictions. In order to obtain the array of channels on a large area a bitmap image was made with 5µm width, spaced 5µm and 0.9mm length. The depth of excavation was set at 80 nm. The image is then replicated by FIB and reproduced on the surface of ZnO films (Fig. 18), milling an area of 0.8mm^2 and covering, consecutively , thanks to the automatic movement of the stage and the ion beam on the sample, the total area (0.5 cm^2) . On the substrate structured glass/TCO, pin single junction amorphous silicon device has been then realized. The spectral response of the solar cell was compared to that measured on a similar device realized on a flat region of the same substrate. The electrical parameters of the two devices, evaluated by measuring the IV characteristics, ensure that FIB does not alter the electrical properties of TCO during the milling process. The measurements of spectral response, shown in Figure 19, do not show any improvement on the textured substrate, as expected because of channel sizes and distances between them are far from theoretical predictions. Work is in progress for reducing the channel dimensions and for verifying the simulation work .

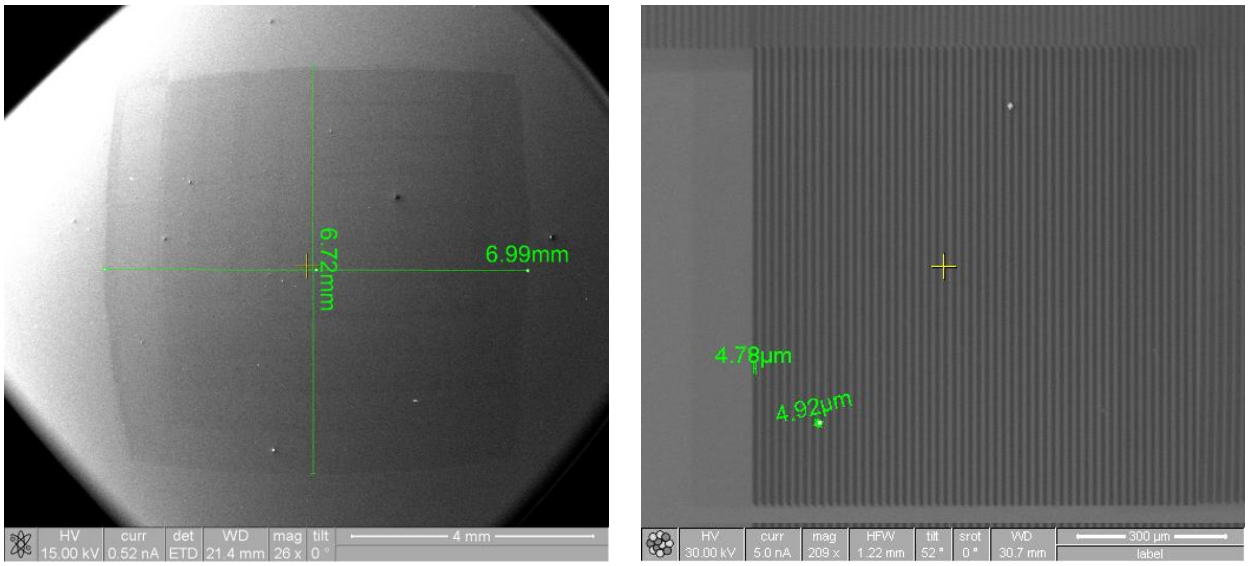

(a) (b)

Figure 18. (a) total area after FIB milling; (b) dimensions and width of channels milled by FIB

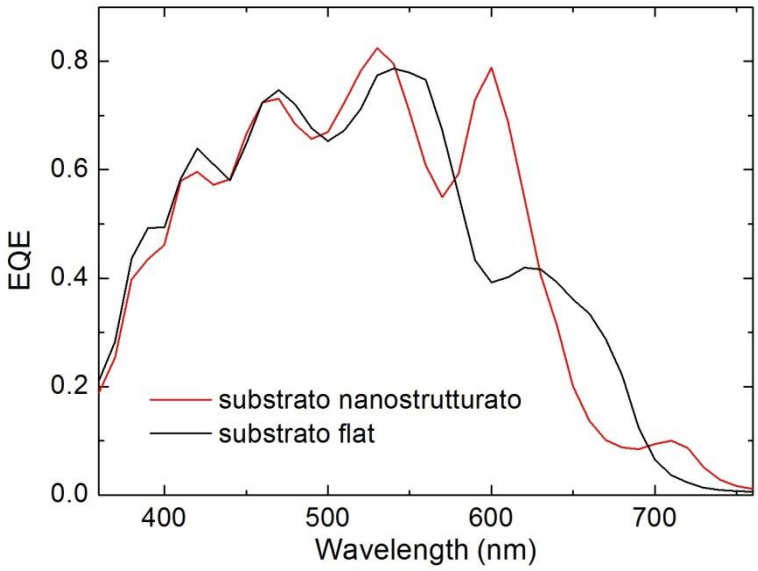

Figure 19. external quantum efficiency measured on cells starting from structured (red) and flat (dark) ZnO layers

3 Conclusions

In conclusion, in this work we have evaluated and compared the performance of backreflectors based on 1-D periodic and Fibonacci aperiodic metal nanograting for light absorption enhancement in thin film (~200 nm) amorphous silicon solar cell. The comparison has been carried out taking into account a realistic model of solar cell including a thin doped silicon oxide (n-SiO_x) layer placed between the nanograting and the active region of the cell, based on a novel design for the rear side of the solar cells. Our results reveal that patterned backreflectors guarantee a significant absorption enhancement if the grating profile is retained on both the top and bottom sides of the active region. In this case, through an exhaustive parametrical analysis of light absorption as a function of the equivalent period and duty cycle for both periodic and Fibonacci grating backreflectors, we found that nanostrucured metallic backreflectors are able to improve up to 20% the light absorption with respect to a simple flat metal mirror. Compared to the periodic case, the Fibonacci-like grating guarantees an enhancement of ~4% by virtue of its denser Bragg spectrum which allows to reach the phase matching condition over more wavelengths and thus the higher capability to spectrally locate multiple resonances. This property also makes the aperiodic backrefleflector more robust with respect to variation of the incoming light incidence angle.

We have also observed that the backreflector pattern is fully efficient only if the appropriate light absorber is selected, with non-zero extinction coefficient within the near-infrared wavelength range, where most of the coupling process of both plasmonic and photonic modes (responsible for the light trapping and enhancement when nanogratings are employed) takes place. As a consequence, we anticipate a strong potential with the application of such nanopatterned reflectors to materials with lower bandgap than a-Si:H, like the µc-Si:H in use in the bottom component of multi-junction solar cells, that currently retains the efficiency records for the thin film Si technology [43].

Overall, our results show that backreflectors based on aperiodic patterns should be preferred in that contexts where even a few percent more of absorption is desirable. In this framework, intriguing perspectives can be envisaged by taking into account the proper selection of the aperiodic pattern to control number, spectral position and mode distribution of resonant modes involved in the light trapping process.

Concerning experimental results n-SiO_x:H films grown on glass substrates by PECVD were patterned by focused ion beam technique for light trapping applications. Different focused ion beam milling conditions, such as ion beam currents, milling times, dwell times, etc., have been explored in order to obtain the desired box-shape for the nanochannels, by reducing the effect of redeposition. Parallel scan with “bottom

to top" direction has been settled. Best magnification and dwell time at $1\mu s$ have been chosen. It has also been important to find the right ion dose, chosen in a precise ion beam current. A quite similar box-shaped nanochannel can be obtained by working at $3x10^{17}$ ions/cm^2 dose. The evaluation of the sputtering yield, both theoretically and experimentally, could help to find the better working conditions to obtain a smaller redeposition, but it does not predict the shape of the nanochannel. It would be interesting to use a code capable of simulating the surface topography in 2D and 3D space, including angle dependent sputtering and redeposition, for obtaining precise pattern shapes. In the final part of the experimental activity ZnO layers have been nanopatterned to verify the feasiblity of FIB milling on this configuration. The nanopatterned area, equal to 0.5 cm^2 , large region for the FIB technology, has been patterned using geometric parameters different from simulation work, for reducing the milling time. The measurements of spectral response do not show any improvement on the textured substrate, as expected because of channel sizes and distances between them are far from theoretical predictions. At the same time the FIB milling does not corrupt the IV characteristics of the structured glass/TCO substrate. In conclusion the work follows the objectives set for silicon thin film devices. Architectures have been designed to improve the absorption of solar radiation and preliminary tests have been performed for realizing solar cells on these structures. Using these results it will be possible to realize other prototypes with advanced light trapping effects by FIB technology, which permits to obtain nanopatterned devices without using a resist layer or etching mask.

4 References

1. A. V. Shah, H. Schade, M. Vanecek, J. Meier, E. Vallat-Sauvain, N. Wyrsch, U. Kroll, C. Droz, and J. Bailat, Prog. Photovolt: Res. Appl. **12**, 113–142 (2004).
2. M. Vanececk, O. Babchenko, A. Purkrt, J. Holovsky, N. Neykova, A. Poruba, Z. Remes, J. Meier, U. Kroll, App. Phys. Lett **98**, 163503 2011..
3. C. Battaglia, J. Escarré, K. Söderström, M. Charrière, M. Despeisse, F.J. Haug, C. Ballif, Nature Photonics **5**, 535-538 (2011).
4. C. Rockstuhl, S. Fahr, K. Bittkau, T. Beckers, R. Carius, F.J. Haug, T. Söderström, C. Ballif, F. Lederer, Opt. Express **18**, 335-341 (2010).
5. O. Isabella, J. Krč, M. Zeman, App. Phys. Lett. **97**, 101106 (2010).
6. H. Sai, H. Jia, M.J. Kondo, J. App. Phys. **108**, 044505 (2010).
7. J. I. Owen, J. Hüpkes, H. Zhu, E. Bunte,. S. E. Pust, Physica Status Solidi A **208**, 109-113 (2011).
8. M. Boccard, C. Battaglia, S. Hänni, K. Söderström, J. Escarré, S. Nicolay, F. Meillaud, M. Despeisse, C. Ballif, Nano Letters **12**, 1344–1348 (2012).
9. E. Moulin, U.W. Paetzold, K. Bittkau, J. Owen, J. Kirchhoff, A. Bauer, R. Carius, Prog. Photovolt.: Res. Appl. **10**, 2355 (2013).
10. M. Peters, M. Rüdiger, H. Hauser, M. Hermle, B. Bläsi, Prog. Photovolt: Res. Appl. **20**, 862–873 (2012).
11. A. Čampa, O. Isabella, R. van Erven, P. Peeters, H. Borg, J. Krč, M. Topič, M. Zeman, Prog. Photovolt: Res. Appl. **18**, 160–167 (2010).
12. P. Delli Veneri, L.V. Mercaldo, I. Usatii, App. Phys. Lett. **97**, 023512 (2010).
13. P. Delli Veneri, L.V. Mercaldo, I. Usatii, Prog. Photovolt.: Res. Appl. 21, 148 (2013).
14. P. Bermel, C. Luo, L. Zeng, L. C. Kimerling, J.D. Joannopoulos, Opt. Express **15**, 16986–17000 (2007).
15. D. Zhou, R. Biswas, J. App. Phys. **103**, 093102 (2008).
16. D.C. Johnson, I. Ballard, K.W.J. Barnham, D.B. Bishnell, J.P. Connolly, M. C. Lynch, T. N. D. Tibbits, N. J. Ekins-Daukes, M. Mazzer, R. Airey, G. Hill, J.S. Roberts, Sol Energy Mater Sol Cells **87**, 169-179 (2005).
17. P. G. O'Brien, N. P. Kherani, A. Chutinan, G. A. Ozin, S. John, and S. Zukotynski, Adv. Mater. **20**, 1577–1582 (2008).
18. A. Bozzola, M. Liscidini, L. C. Andreani, Opt. Express **20**, 224–244 (2012).
19. S. A. Maier, *Plasmonics: Fundamentals and applications* (Springer: Berlin, 2007).
20. H. A. Atwater, A. Polman, Nature. Mater. **9**, 205–213 (2010).
21. W. Wang, S. Wu, K. Reinhardt, Y. Lu, S. Chen, Nano Lett. **10**, 2012–2018 (2010).
22. V. E. Ferry, M. A. Verschuuren, M. C. van Lare, R. E. I. Schropp, H. A. Atwater, and A. Polman, Nano Lett. **11**, 4239–4245 (2011).
23. C. Battaglia, C. M. Hsu, K. Söderström, J. Escarré, F. J. Haug, M. Charrière, M. Boccard, M. Despeisse, D. T. Alexander, M. Cantoni, Y. Cui, C. Ballif, ACS Nano **27**, 2790-7 (2012).
24. M. Senechal, *Quasicrystals and geometry*, (Cambridge University Press: Cambridge, UK, 1995).
25. J.B. Suck, M. Schreiber, P. Häussler, *Quasicrystals: an introduction to structure, physical properties, and applications* (Springer: Berlin, 2002).
26. A. Ricciardi, M. Pisco, A. Cutolo, A. Cusano, L. O'Faolain, T. F. Krauss, G. Castaldi, V. Galdi, Phys. Rev. B **84**(8), 085135 (2011).
27. J. Trevino, C. Forestiere, G. Di Martino, S. Yerci, F. Priolo, L. Dal Negro, Optics Express **20**, A418-A430 (2012).
28. A. Crescitelli, A. Ricciardi, M. Consales, E. Esposito, C. Granata, V. Galdi, A. Cutolo, and A. Cusano, Adv. Funct. Mater. **22**, 4389-4398 (2012).
29. E. Macià, Rep. Prog. Phys. **75**, 036502 (2012).
30. G. Yue, L. Sivec, J.M. Owens, B. Yan, J. Yang, S. Guha, Applied Physics Letters **95,** 263501 (2009)
31. H.B.T. Li, R.H. Franken, J.K. Rath, R.E.I. Schropp, Solar Energy Materials & Solar Cells **93,** 338–349 (2009)

32. M. Python, D. Dominé , T. Söderström, F. Meillaud, C. Ballif, Prog. Photovolt: Res. Appl. **18** 491–499 (2010)
33. M. Steltenpool, J. Rutten, G. van der Hofstad, H. de Groot, A. Tavakoliyaraki, A.J.M. van Erven and G. Rajeswaran, Proceedings of the 27th EU-PVSEC, 2123-2128 (2012)
34. G. Bugnon, G. Parascandolo, T. Söderström, P. Cuony, M. Despeisse, S. Hänni, J. Holovský, F. Meillaud, C. Ballif, Adv. Funct. Mater. **22**, 3665–3671,(2012)
35. www.comsol.com.
36. E. D. Palik, *Handbook of Optical Constants of Solids,* Academic Press (1997).
37. NREL, "ASTM (G-173-03)," http://rredc.nrel.gov/solar/spectra/am1.5/
38. Jager K., Zeman M., *Appl. Phys. Lett*. **95**: 171108 (2009).
39. R.A. Dunlap, *The Golden Ratio and Fibonacci Numbers,* (World Scientific Publishing Co.Pte.Ltd., 1997).
40. Sopra N&K Database (Sopra Group, Belfast, Ireland), http://www.sopra-sa.com/index2.php?goto=dl&rub=4
41. L.T. Wong, W.K. Chow, Solar radiation model, Appl. Energy **69**, 191–224 (2001).
42. D. King, J. A. Kratochvil, W. E. Boyson, Measuring Solar Spectral and angle-of Incidence Effects on PV Modules and Solar Irradiance Sensors, *26th IEEE PVSC* 1997, 1113-1116.
43. S. S. Wang, R. Magnusson, Appl. Opt. **32**, 2606-2613 (1993).
44. L. Frey, C. Lehrer, and H. Ryssel, Nanoscale effects in focused ion beam processing. *Appl. Phys. A* 76, (2003) 1017-1023.
45. W. C. L. Hopman, F. Ay, W. Hu, V. J. Gadgil, L. Kuipers, M. Pollnau and R. M., de Ridder, Focused ion beam scan routine, dwell time and dose optimizations for submicrometer period planar photonic crystal components and stamps in silicon. *Nanotechnology* 18 (2007) 195305(1)- 195305(11).
46. M. Shridhar, D.K. Maurya, J.R. Friend, and L.Y. Yeo, Focused ion beam milling of microchannels in lithium niobate, *Biomicrofluidics* 6, (2012) 012819(1)- 012819(11).
47. M. Kolibal, T. Matlocha, T. Vystavel and T. Sikola, Low energy focused ion beam milling of silicon and germanium nanostructures, *Nanotechnology* 22, (2011) 105304(1)- 105304(8).
48. Y. Tanaka, T. Asano, Y. Akahane, B. S. Song and S. Noda, Theoretical investigation of a two-dimensional photonic crystal slab with truncated cone air holes, *Appl. Phys. Lett.* 82, (2003), 1661–1663.
49 . Y. Q. Fu, N. K. A. Bryan, O. N. Shing, and N. P. Hung, Influence of the Redeposition effect for Focused Ion Beam 3D Micromachining in Silicon*, Int. J. Adv. Manuf. Technol*. 16, (2000), 877-880.
50 . B.I. Prenitzer, C.A. Urbanik-Shannon, L.A. Giannuzzi, S.R. Brown, R.B. Irwin, T.L. Shofner, and F.A. Stevie The correlation between ion beam/material interactions and practical FIB specimen preparation, *Microsc. Microanal*. 9, (2003) 216-236.
51. J.F. Ziegler, J.P. Biersack, and U. Littmark, The Stopping Range of Ions in Solids (Pergamon Press, New York, 1985). The SRIM code is available online at www.srim.org
52. S. Mirabella, G. Di Martino, I. Crupi, S. Gibilisco, M. Miritello, R. L. Savio, M. A. Di Stefano, S. Di Marco, F. Simone, and F. Priolo, Light absorption and electrical transport in Si:O alloys for photovoltaics, *J. Appl. Phys.* 108, (2010) 093507 (7 pages).
53. C.A. Volkert and A.M. Minor, Focused Ion Beam Microscopy and Micromachining, *MRS bulletin*, 32, (2007) 389-395
54. H. X. Qian, W. Zhou, X. M. Li, J. M. Miao and L. E. N. Lim, Accurate detection of interface between SiO2 film and Si substrate, *Appl. Surf. Sci*., 253, (2007) 5511–5515.
55. O. Wilhelmi, S. Reyntjens, C. Mitterbauer, L. Roussel, D. J. Stokes, and D. H. W. Hubert, Rapid Prototyping of Nanostructured Materials with a Focused Ion Beam, *Jap. J. Appl. Phys.*. 47, (2008) 5010–5014 .
56 . A. A. Tseng, I. A. Insua, J. S. Park, B. Li, and G. P. Vakanas, Milling of submicron channels on gold layer using double charged arsenic ion beam, *J. Vac. Sci. Technology* B 22, (2004) 82-89.
57. H.W. Li, D. J. Kang, M. G. Blamire, and W. T. S. Huck, Focused ion beam fabrication of silicon print masters, *Nanotechnology* 14, (2003) 220–223.

58. Y. Liu Rapid nano-patterning of polymeric thin films with a gallium(+) focused ion beam, PhD Thesis, University of Virginia, Virginia (2005)
59. M. P. Seah and T. S .Nunney, Sputtering yields of compounds using argon ions, *J. Phys. D: Appl. Phys.* 43, (2010) 253001 (13pp)
60. L. Bischoff and J. Teichert, Focused Ion Beam Sputtering of Silicon and Related Materials, http://www.hzdr.de/publications/001143/1143.pdf
61. H.B. Kim, G. Hobler, A. Steiger, A. Lugstein and E. Bertagnolli, Full three-dimensional simulation of focused ion beam micro/nanofabrication, *Nanotechnology* 18, (2007) 245303 (8pp).
62. C. Ebm, E. Platzgummer, H. Loeschner, S. Eder-Kapl, P. Joechl, M. Kuemmel, R. Reitinger, G. Hobler, A. Koeck, R. Hainberger, M. Wellenzohn, F. Letzkus and M. Irmscher, Ion multibeam nanopatterning for photonic applications: Experiments and simulations, including study of precursor gas induced etching and deposition, *J. Vac. Sci. Technol. B* 27, (2009) 2668-2673

5 CV of the University Investigators

Andrea Cusano was born on May 31, 1971, in Caserta. He received his Master degree cum Laude in Electronic Engineering on November 27, 1998 from University of Naples "Federico II", Italy and his Ph.D. in "Information Engineering" from the same university, with tutor Professor Antonello Cutolo. He is actually Associate Professor at the University of Sannio, Benevento. From 1999 his activity is focused in the field of optoelectronic devices for sensing and telecommunication applications. He was cofounder in 2005 of the spin-off company "OptoSmart S.r.l." and in 2007 of the spin-off company "MDTech". He published over 100 papers on prestigious international journals and more than 150 communications in well known international conferences worldwide; he has 4 international patents currently in charge of prestigious industrial companies (Ansaldo STS, Alenia WASS, Optosmart and MdTEch) and more than 10 national patents. He is also referee of several scientific international journals. He is associate editor of Sensors and Transducers Journal, Journal of Sensors (Hindawi), The Open Optics Journal (Bentham),The Open Environmental & Biological Monitoring Journal (Bentham) and the International Journal on Smart Sensing and Intelligent Systems. He is a member of the technical committee of several international conferences such as IEEE Sensors, ICST, EWSHM, EWOFS. Andrea Cusano was principal investigator and scientific responsible of several national and international research projects. He is coauthor of more than 10 chapters published in international books and invited papers in prestigious scientific international journals. He is coeditor of 2 Special Issues (Special Issue on Optical Fiber Sensors, IEEE Sensors 2008, and Special Issue on "Fiber Optic Chemical and Biochemical Sensors: Perspectives and Challenges approaching the Nano-Era", Current Analytical Chemistry, Bentham, 2008. and of 3 scientific international books. He is also consultant for big companies of the Finmeccanica group such as Ansaldo STS and Alenia WASS. He has also collaborations with CERN in Geneva where he is working on the development of innovative sensors for high energy physics applications.

Marco Pisco was born in Naples, Italy on 1977. He received the information and telecommunication engineering degree in 2003 from the University of Naples Federico II, Italy. He finished his international Ph.D. course at the University of Sannio, Italy, in joint with the Faculty of Electrical Engineering (FER) at the University of Zagreb in 2007. Currently he is a postdoctoral researcher at the Optoelectronic Division - Engineering Department of the University of Sannio. His field of interest is in the area of optoelectronic sensors and photonic bandgap based devices for sensing and communication applications. He is author and co-author of several international publications, including international journals, conferences and books' chapters and reviewer for IEEE, OSA and Elsevier journals.

Armando Ricciardi graduated from University of Sannio (Italy) in Telecommunication Engineering in 2006. He received his Ph.D. in Information Engineering from the University of Naples "Parthenope", in 2010. He spent a half of his Ph.D. at the Microphotonics Group of the St Andrews University in Scotland. From January 2011 he is a post-doc student at the optoelectronic division of the Engineering Department of University of Sannio.
His current research activity essentially focuses on the theoretical analysis and design of Photonic Crystals optical devices for a wide range of applications, including:
-Backreflectors in thin film Solar Cells
-Lab on Fiber Technology
- Hybrid Plasmonic-Photonic structures for biosensing

Giuseppe Quero was born on August 25, 1981 in Taranto, Italy. He received the B.S. and M.S. degree in Telecommunications Engineering from University of Sannio, Benevento, Italy, in January 2006 and December 2008 respectively. He received his Ph.D. in Information Engineering from the University of Sannio in 2012.In October 2010, he won of the "EWOFS'2010 Student Paper Award" in the Fourth European Workshop in Optical Fibre Sensors.
His research interests essentially include-micro and nano-lithography techniques for fiber based optoelectronic devices.

Alberto Micco was born on March 7, 1985 in Benevento, Italy. He graduated from University of Sannio (Italy) in Telecommunication Engineering in 2011. From July 2012, he is attending a PhD course in Information Engineering at University of Sannio.
His research interests essentially include the design of backreflectors in thin film Solar Cells and nanostructures to be integrated on optical fibers.